Optics & Laser Technology 187 (2025) 112764



Contents lists available at ScienceDirect

Optics and Laser Technology

journal homepage: www.elsevier.com/locate/optlastec

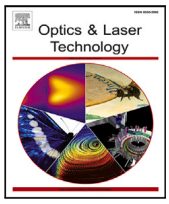

Full length article

Improved wavefront reconstruction for Shack–Hartmann wavefront sensor in the presence of shock-related distortions

Ethan D. Chu *, Timothy J. Bukowski, Stanislav Gordeyev

University of Notre Dame, Hessert Laboratory for Aerospace Research, South Bend, 46637, IN, United States of America

ARTICLE INFO

Keywords:
Wavefront reconstruction
Shack–Hartmann
Digital holography
Diffraction-limited dot
Supersonic shock
Density gradient

ABSTRACT

Previous research has demonstrated that large density gradients, such as those produced by supersonic shockwaves, adversely affect the wavefront reconstruction of Shack–Hartmann wavefront sensors (SHWFS). Shocks cause non-diffraction-limited irradiance patterns, leading to incorrect local tilt measurements by SHWFS, and, as a consequence, degraded reconstructed wavefront accuracy. To study the effect of shocks on the reconstruction accuracy of SHWFS, experimental wavefront measurements were performed, when the interrogating laser beam was propagated along a local shock formed in transonic flow over a partial cylinder. The resulting wavefronts were simultaneously measured by a SHWFS and a digital holography wavefront sensor (DHWFS) and then compared, treating the DHWFS as the "ground truth." Significant error was found in the SHWFS measurements, with the error increasing nonlinearly with shock strength. Three metrics, specifically standard deviation, kurtosis, and slope discrepancy, were evaluated for their effectiveness in identifying the dots, distorted by the local shock. Excluding points that exceeded a set threshold significantly improved wavefront accuracy. A complete SHWFS wavefront was then recovered by filling in the excluded points with a spline interpolation. This algorithm decreased the root mean squared error of the SHWFS wavefront by around 30% on average. These findings contribute to the advancement of shock-wave-tolerant phase reconstruction algorithms and introduce a method for more accurate wavefront recovery in the case where a shock partially crosses the aperture.

1. Introduction

The Shack–Hartmann Wavefront Sensor (SHWFS) was initially developed by Johannas Franz Hartmann who used an opaque screen with an array of holes. This was further developed by Roland Shack and Ben Platt in 1971 [1] who exchanged the screen with an array of micro lenses. The development of the SHWFS was motivated by the need to accurately measure and correct optical aberrations in telescopes, particularly in astronomical observations. The SHWFS has broad applications in ophthalmology [2], optical testing and alignment [3,4], and microscopy [5,6], to name a few. The SHWFS has found widespread use in adaptive optics systems, which are employed to correct for atmospheric turbulence and other aberrations in real-time [7–11]. By continuously monitoring the wavefront distortions and feeding the information to deformable mirrors, adaptive optics systems can dynamically correct for these aberrations, resulting in sharper images and improved resolution in various optical applications [12]. The SHWFS is also used extensively as a non-intrusive method to investigate flow-field density via measuring related wavefronts. In this case, all data are post-processed, and accuracy is prioritized over speed [13–15].

In a SHWFS, a lenslet array is used to break down an incoming aberrated laser beam into a series of smaller beams. Each beam is focused to an image plane, resulting in a series of diffraction-limited dots. The location of the dot depends on the local wavefront gradient over each lenslet subaperture. By carefully measuring the dot locations, the local gradient (slope) of the global wavefront can be estimated, and the wavefront can be reconstructed [16].

There has been a considerable amount of research into the integration of laser propagation systems into airborne platforms [17–20]. A large interest is in higher speed transonic and supersonic flow regimes, where shocks form a sharp density change in the flow, thereby affecting the index of refraction and significantly effecting beam propagation. Kalensky et al. [21,22] have shown that the presence of the shock will result in distorted or bifurcated dots in the image plane. These distorted dots will provide incorrect measurements of the local wavefront slope and, as a consequence, deteriorate the accuracy of the SHWFS.

In the past couple of years, there have been several works published studying the effects of strong density gradient shock waves on Shack–Hartmann wavefront sensor measurements, with the goal of extending

* Corresponding author.
E-mail address: echu3@nd.edu (E.D. Chu).

https://doi.org/10.1016/j.optlastec.2025.112764
Received 17 November 2024; Received in revised form 28 February 2025; Accepted 4 March 2025
Available online 27 March 2025
0030-3992/© 2025 The Authors. Published by Elsevier Ltd. This is an open access article under the CC BY-NC license (http://creativecommons.org/licenses/by-nc/4.0/).

the capability of the SHWFS to accurate measure wavefronts in environments with shocks. Kalensky et al. [22] analytically showed how the density discontinuity of a shock crossing a subaperture lenslet leads to discontinuous phase in the pupil plane, and a bifurcated dot irradiance pattern in the far-field observation plane. One of the first observations of the phenomena was recorded by Panda [23] in experiments done at NASA Glenn Research Center. More recently, Kemnetz experimentally showed these effects can be caused by oblique shocks formed on a wedge in a supersonic flow [24] conducted at Kirtland Air Force Base. Kalensky et al. [22] also showed when the shock is at an angle off-axis with the incoming beam, the wavefront instead follows a more gradual ramp increase across the shock region, leading to a more complicated dot pattern. Then, through wave-optics simulation, it was shown how distorted dots affect wavefront slope estimation and, in turn, wavefront reconstruction [22].

Higher order spatial statistics of the irradiance-patterns have been used before in literature to improve wavefront reconstruction. In Ref. [25] they were related to affine coefficients which were then used to reconstruct the wavefront. Kalensky [26] used the second moment of the irradiance pattern to identify dots distorted by higher order aberration, and, in the particular case of that work, branch points. Slope discrepancy is another metric that has been used to find shock-affected dots in a SHWFS [27].

DeFoor et al. [28] developed an algorithm to improve Shack–Hartmann wavefront reconstruction in the case where there is a shock that crosses the aperture. This algorithm uses the second moment of the dot's irradiance pattern to determine which dots have been affected by the presence of a shock. The wavefront slope across the affected lenslets is then replaced with an improved estimate that uses higher-order information about the irradiance pattern, and the wavefront is then reconstructed. DeFoor et al. [29] used the same algorithm, but trained a neural network to more accurately relate the distorted irradiance pattern to the wavefront slope. A more robust reconstruction algorithm was developed in Ref. [30] which decreases the global effect of the shock-affected tilt measurements on the rest of the wavefront by using special weighting functions. A related study by Yang et al. [31] looked at using an autocorrelation method and a neural network to improve the dynamic range of the SHWFS in high aberration environments simulated with a use of Zernike Polynomials.

In this paper we characterize the effects of shocks on Shack-Hartmann wavefront sensor measurements using experimental measurements of a beam passed through flow over a partial cylinder in transonic flow. This flow field was previously studied in Ref. [32] where complementary computational fluid dynamics (CFD) simulations and wind tunnel experiments were run and compared to characterize the transonic shock that forms over the cylinder. Fig. 1(a) shows their CFD results for the flow field around the cylinder, where the color represents Mach number (velocity normalized by the speed of sound). We can see the flow accelerates over the front of the cylinder up the apex of the turret where the yellow–red region shows the flow is supersonic with a Mach number greater than 1. This local supersonic region is followed downstream by a shock where the flow is compressed, greatly increasing density, and brought back down to subsonic speeds. The shock location has been overlayed on the image with a dashed black line. In the same study experimental data was collected including Schlieren images such as Fig. 1(b) in which the intensity is related to density gradients. Here we can see the shock on top of the turret shown as bright white, which is stronger towards the cylinder surface and grows weaker further from the surface. The same cylinder geometry and wind tunnel used in Ref. [32] are used for the experiment in this paper. Simultaneous measurements using Shack–Hartmann and digital holography wavefront sensors are taken and compared. Since the interferometry-based digital holography wavefront sensor (DHWFS) correctly measures the wavefronts with discontinuities, wavefronts collected by a digital holography wavefront sensor were treated as "ground truth" measurements.

In Section 2 we discuss the theory and equations used for Shack–Hartmann and digital holography wavefront sensors. In Section 3 we describe the experimental setup we used to create a local shock over a semi-cylinder and take simultaneous Shack–Hartmann and digital holography wavefront measurements. Section 4 first compares Shack–Hartmann wavefronts to the digital holography measurements. It then analyzes the Shack–Hartmann images and discusses using higher-order spatial statistics and slope discrepancy to determine the shock-affected dots in the irradiance pattern. The Shack–Hartmann wavefront is reconstructed without the affected dots and compared to digital holography measured wavefronts. This comparison assesses effectiveness of the different methods used to identify affected dots and highlights the global impact these distorted dots have on the wavefront. Lastly, the masked-out regions of the wavefront are filled in by interpolation and compared again to digital holography wavefronts.

Finally, our findings are summarized in Section 5. Before moving on to the next section, it is important to note that the results presented in this paper go well beyond those presented in a recent conference proceeding [33].

2. Sensor wavefront reconstruction

2.1. Shack–Hartmann wavefront sensor

2.1.1. SHWFS wavefront reconstruction

As mentioned in the Introduction, the SHWFS uses a lenslet array to create an array of dots on a sensor to measure a wavefront. For an unaberrated planar wavefront, the diffraction-limited irradiance pattern contains a grid of regularly spaced dots. When the wavefront is disturbed, the individual dots will be displaced from the optical axis of each lenslet, as shown in Fig. 2. Using this displacement, we can approximate the local wavefront slope using simple trigonometry as

$$\left(\frac{\partial w}{\partial x}\right)_k \approx -\left(\theta_x\right)_k = -\frac{\Delta x_k}{f}, \tag{1}$$

$$\left(\frac{\partial w}{\partial y}\right)_k \approx -\left(\theta_y\right)_k = -\frac{\Delta y_k}{f}, \tag{2}$$

where $\left(\frac{\partial w}{\partial x}, \frac{\partial w}{\partial y}\right)$ is the two-dimensional wavefront slope over a subaperture lenslet, $\left(\theta_x, \theta_y\right)$ is the calculated slope, k is the lenslet number, and f is the lenslet focal length. The displacements are measured relative to their position with the wind tunnel off. This automatically removes any steady aberrations related to imperfect optical setup. The wavefront is reconstructed by solving a discretized version of Eq. (2) using the Southwell reconstructor algorithm [34]. Lastly, instantaneous global tip, tilt, and piston components are removed from the reconstructed wavefront.

A key assumption in the wavefront reconstruction process is that the tilt across each lenslet calculated from the shift in the dot position, referred to as a centroid tilt or C-tilt [9], is equal to the tilt of the wavefront at that location. However, when there is a discontinuity across the lenslet, the irradiance pattern bifurcates or smears, and C-tilt is no longer as good of an estimate of wavefront tilt [22]. Since the wavefront is constructed through a least-squares reconstructor, these contaminated tilt measurements affect the accuracy of the entire reconstructed wavefront. There are three main types of reconstructors available: Fried [36], Hudgin [37], and Southwell [34]. However, each of these methods still depend on accurate measurements of the C-tilt. If the C-tilt cannot be used, then none of the reconstructors will produce an accurate wavefront. Thus, the approach of this work is to identify and remove distorted dots. This leaves the well-defined diffraction-limited dots to calculate the wavefront using any selected reconstructor. The removed points are interpolated in and a full wavefront is obtained.

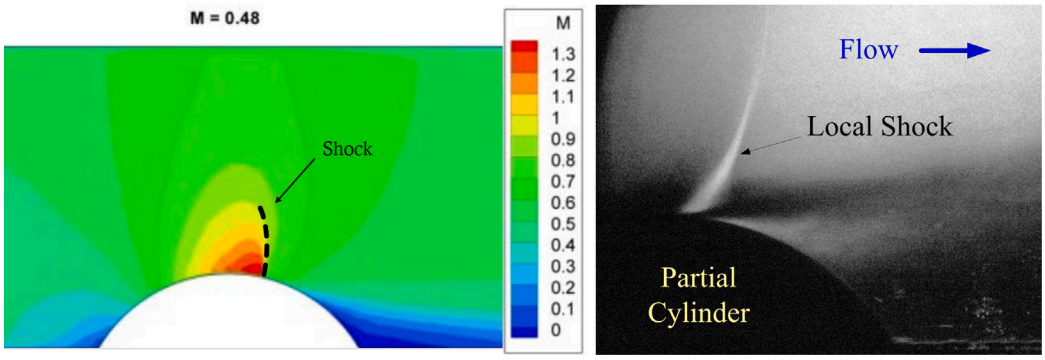

Fig. 1. (a) CFD simulations showing transonic flow over the partial cylinder with the shock marked by a dashed line.(b) Spanwise Schlieren image of the transonic flow over the partial cylinder with a local shock.
Source: Both (a) and (b) are adapted from [32].

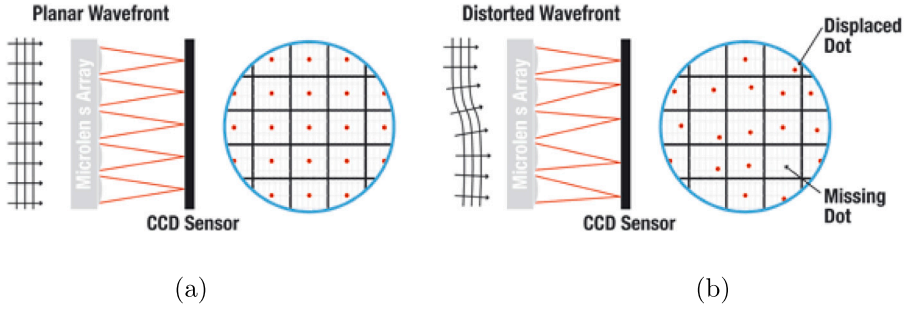

Fig. 2. Principle of operation of Shack–Hartmann WFS works by observing the displacement of the dots in a lenslet array. (a) For a planer wavefront, the dots on the image plane are regularly spaced. (b) When a distorted wavefront is passed through the lenslet array, the dots are displaced by some measurable amount.
Source: Thorlabs.com [35].

2.1.2. *Farfield spatial statistics*

In Refs. [26] and [28] the spread in irradiance patterns caused by higher order aberration across the lenslet was quantified using the second central moment. Through this approach, we can identify which dots have been distorted by the shock-related large wavefront gradients and exclude them from the reconstruction, thereby increasing accuracy. The ultimate goal would then be to go back and use additional information to reconstruct the wavefront at the excluded points. In this paper, we extend this idea of using moments to identify these distorted dots. We show that using the second and fourth central moments, and slope discrepancy, we are able to identify the contaminated irradiance patterns with each area of interest (AOI).

The traditional Shack–Hartmann wavefront analysis breaks the irradiance pattern into AOI behind each lenslet. The centroid of the dot within each AOI can then be calculated to find the dot displacement [38]. The centroid is calculated as

$$\overline{x} = \frac{\int_{-\infty}^{\infty}\int_{-\infty}^{\infty} I(x,y)\, x\, dxdy}{\int_{-\infty}^{\infty}\int_{-\infty}^{\infty} I(x,y) dxdy}, \quad \text{and} \quad \overline{y} = \frac{\int_{-\infty}^{\infty}\int_{-\infty}^{\infty} I(x,y)\, y\, dxdy}{\int_{-\infty}^{\infty}\int_{-\infty}^{\infty} I(x,y) dxdy}, \tag{3}$$

where $I(x,y)$ is the intensity of each pixel, x and y are the location of the pixel within the AOI, and $\overline{x}$ and $\overline{y}$ are the relative locations of the centroid. This is also referred to as the first moment of the distribution within the AOI. The second central moment, sometimes called the variance, is more commonly used in the form of standard deviation and is found by

$$\mu_{2,x} = \frac{\int_{-\infty}^{\infty}\int_{-\infty}^{\infty} I(x,y)\,(x-\overline{x})^2\, dxdy}{\int_{-\infty}^{\infty}\int_{-\infty}^{\infty} I(x,y) dxdy} \quad \text{and} \quad \sigma_x = \sqrt{\mu_{2,x}} \tag{4}$$

where $\mu_{2,x}$ is the second central moment in x-direction and σ_x is the standard deviation in x-direction [39]. The same process is applied to the y direction. This quantity represents the relative width of the intensity distribution in the x and y direction. This is applied to each AOI. The x and y components are added in quadrature to obtain a unified value. The σ map is then normalized by the no-flow case such that,

$$\sigma_{Norm} = \frac{\sigma_F - \sigma_{NF}}{\sigma_{NF}} \tag{5}$$

where σ_{Norm} is the normalized standard deviation, σ_F is the standard deviation of the flow-with-shock condition, and σ_{NF} is the standard deviation of the no-flow condition.

The third central moment gives us the skewness of the distribution within the AOI. Skewness describes an asymmetry of the irradiance pattern. This is defined by the following

$$\mu_{3,x} = \frac{\int_{-\infty}^{\infty}\int_{-\infty}^{\infty} I(x,y)\,(x-\overline{x})^3\, dxdy}{\int_{-\infty}^{\infty}\int_{-\infty}^{\infty} I(x,y) dxdy} \quad \text{and} \quad Skew_x = \frac{\mu_{3,x}}{\sigma_x^3} \tag{6}$$

where $\mu_{3,x}$ is the third central moment in x-direction and $Skew_x$ is the skewness in x-direction [39]. Skewness shows asymmetry in the intensity distribution pattern, and is more of a measurement of how much the peak is shifted from the mean. Skewness was explored as a metric for identifying distorted dots in [33], however, it did not provide a clear distinction between diffraction-limited dots and distorted dots.

The fourth central moment is used to identify the "tailedness" of the distribution; that is a measure that relates to the tails of a distribution. Higher kurtosis values indicate a greater presence of extreme deviations (or outliers) in the data. In the presence of a sharp gradient, the dots are usually distorted in some extreme fashion which increases the presence of these outliers. Kurtosis allows us to quantify the "spread" of the distribution for these distorted dots. This is defined as

$$\mu_{4,x} = \frac{\int_{-\infty}^{\infty}\int_{-\infty}^{\infty} I(x,y)\,(x-\overline{x})^4\, dxdy}{\int_{-\infty}^{\infty}\int_{-\infty}^{\infty} I(x,y) dxdy} \quad \text{and} \quad Kurt_x = \frac{\mu_{4,x}}{\sigma_x^4} \tag{7}$$

where $\mu_{4,x}$ is the fourth central moment and $Kurt_x$ is the kurtosis in x-direction [39]. The x and y components are added in quadrature to give a single value. In further discussions, $Kurt$ refers to the relative kurtosis as it has been normalized by σ. Kurtosis is similar to standard deviation in that is looks at the distribution of the intensity to identify the "bad" dots. However, it is more sensitive to changes away from the mean. Normalizing by the no-flow, we can eliminate some of the noise caused by the system itself and is defined by Eq. (8).

$$Kurt_{Norm} = \frac{Kurt_F - Kurt_{NF}}{Kurt_{NF}} \tag{8}$$

where $Kurt_{Norm}$ is the normalized value of kurtosis, $Kurt_F$ is the kurtosis of the flow-with-shock condition, and $Kurt_{NF}$ is the kurtosis of the no-flow condition.

2.1.3. Slope discrepancy

Slope discrepancy is a metric first introduced in Ref. [40] which compares measured wavefront slopes to the slopes of the reconstructed wavefront. It is known that subaperture fitting error, measurement noise, and discontinuities such as branch points or shock waves all contribute to slope discrepancy, which means it should be a valuable tool for locating the shock in the aperture. Following Ref. [41], slope discrepancy can be defined as

$$\delta = \theta - \Gamma H \theta \tag{9}$$

where θ is the measured slope vector from the Shack–Hartmann sensor, Γ is the phase reconstructor operator, and H is the pseudo-inverse of the operator Γ. This definition can be more simply written in its x and y components as

$$\delta_x = \theta_x + \frac{\partial w}{\partial x}, \quad \delta_y = \theta_y + \frac{\partial w}{\partial y} \tag{10}$$

where w is the reconstructed wavefront. The x and y components are added in quadrature to give a single slope discrepancy value.

2.2. Digital holography wavefront sensor

While the SHWFS measures the wavefront slopes, digital holography wavefront sensors (DHWFS) allow us to directly measure the complex optical field of the beam. Our setup uses an off-axis pupil plane recording geometry where the signal beam interferes with a tilted planar reference beam onto a camera sensor, creating a fringe pattern hologram or intensity field. An example image is shown in Fig. 3(a) with a zoomed in window showing the fringe pattern. This process is described in further detail in [42–44].

The total intensity of the fringe pattern, I, is the superposition of the complex optical fields of the signal and reference beams, U_S and U_R, respectively. This is defined as

$$I = |U_S + U_R|^2 = |U_S|^2 + |U_R|^2 + U_S U_R^* + U_S^* U_R.$$

$|U_S|^2$ and $|U_R|^2$ are the zeroth-order terms which are ignored as they do not contribute to the phase information [45]. $U_S U_R^*$ and $U_S^* U_R$ contain the phase information we desire. The $(*)$ denotes complex conjugates, thus $U_S U_R^*$ and $U_S^* U_R$ are simply complex conjugates of each other and we only need one pair to find the optical complex field. To isolate one term, $U_S U_R^*$, we perform a Fourier transform on the hologram capture on the camera sensor, shown in Fig. 3(a). The result is presented in Fig. 3(b). We can then filter out all the other unwanted terms (i.e. $U_S^* U_R$, $|U_S|^2$ and $|U_R|^2$) by selecting only the off-axis peak circled in red in Fig. 3(b).

Mathematically this process goes as follows: The signal and conjugate of the reference beam have the complex optical fields

$$U_S(x, y) = A_S \exp[i\phi_S(x, y)]$$

and

$$U_R^*(x, y) = A_R \exp[-i\phi_R(x, y)] \exp\left[-i\frac{2\pi}{\lambda}(x_R + y_R)\right] \tag{11}$$

where A_S and A_R are the amplitude of the signal and reference beam, respectively, (x, y) correspond to the coordinate system at the pupil plane incident on the camera sensor, ϕ_S and ϕ_R are the phase of the signal and reference beams, λ is the laser wavelength, and (x_R, y_R) are the tilt terms induced on the reference beam. After isolating $U_S U_R^*$, we remove tip/tilt component introduced by the reference beam by shifting it to the middle of the Fourier plane, then perform the inverse Fourier transform.

$$\mathscr{F}^{-1}\{U_S U_R^*\} = \mathscr{F}^{-1}\left\{A_S A_R \exp[i(\phi_S - \phi_R)] \exp\left[i\frac{2\pi}{\lambda}(x_R + y_R)\right]\right\}$$

This is done first for a "no flow" case with the tunnel off to get the complex optical field of the imperfect optics system, which we can then remove from the flow on cases. The resulting amplitude and phase fields are shown in Figs. 4(a) and 4(b). However, at this point the phase is wrapped between $-\pi$ and π and must be unwrapped before it can be related to wavefront. As with the SHWFS, the remaining instantaneous global tip, tilt, and piston components are then removed from the wavefront.

In unwrapping the phase, the method used was developed by Herráez et al. [46] and prioritizes unwrapping based on pixel reliability. This method works well for relatively smooth phase patterns such as the no-flow case. However, with more complicated phase patterns or increased noise, this method will incorrectly unwrap in some spots, leaving behind patchy discontinuities which can be seen in Fig. 4(c) near the center of the frame. Filtering the complex optical field was attempted to try to decrease noise and to better unwrap the phase, but it only had a marginal effect. We chose the Herráez method, as the local error associated with points missed during unwrapping are much more obvious. By calculating the spatial derivative of the unwrapped wavefront, we got a metric of how many phase wraps the algorithm missed and discarded any frames that were poorly unwrapped. A least-squares method for unwrapping was also researched but this was found to have more error, especially near the shock. More of this discussion can be found in Ref. [33].

3. Experimental setup

The wind tunnel used in the experiments is located at the Hessert Laboratory for Aerospace Research at the University of Notre Dame. It is an indraft tunnel driven by up to two fans with variable speeds with a 102 × 102 × 305 mm (4 × 4 × 12 inch) test section. The facilities were described in detail in Refs. [32] and [47] and an interested reader is referred to these references for a complete discussion. In order to create a shock, a partial cylinder with a 100 mm diameter curvature and 25 mm height, was installed in the test section shown in Fig. 5(a). The cylinder locally accelerates the flow to supersonic speeds to produce a localized shock at its peak. The size and strength of this shock, and thus the degree of the resulting wavefront local gradient in the shock area, can be adjusted by increasing or decreasing the flow speed. For our system, the critical freestream Mach number for a local shock to appear above the partial cylinder was about Mach 0.45. Mach numbers 0.43–0.48 were tested with corresponding freestream speeds of around 140–160 m/s. The partial cylinder and wind tunnel used here are the same as those used in Ref. [32].

The schematic of the experimental setup is presented in Fig. 5(b). The laser emitter used was a Torus 532 nm green laser. The collimation tube expands the pencil beam of 1.7 mm (≈ 1/16 in) into a 25.4 mm (1 in) beam. BC1 splits the beam into the reference beam for the DHWFS and the signal beam. Passing the signal beam through L1(f200) and L2(f400) expands the beam to 51 mm (2 in). After passing through the test section, L3(f700) and L4(f285) reduces the beam to about 20 mm. An iris is placed at the focal point of the reimaging telescope L5(f250) and L6(f250) to eliminate ghosts from back reflections. BC2 splits the signal beam for the SHWFS and the DHWFS. The reference beam is expanded using L7(-f250) and L8(f500) and combined with the signal

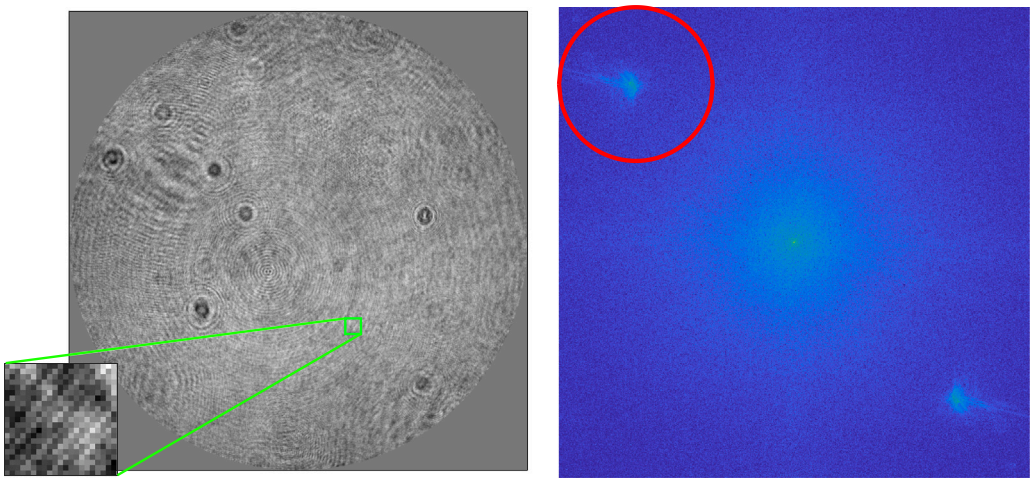

(a) (b)

Fig. 3. (a) Example recorded hologram with zoomed in window showing fringes. (b) 2-dimensional Fourier transform of the hologram with logarithmic color scale. Only the region circled in red is kept for analysis.

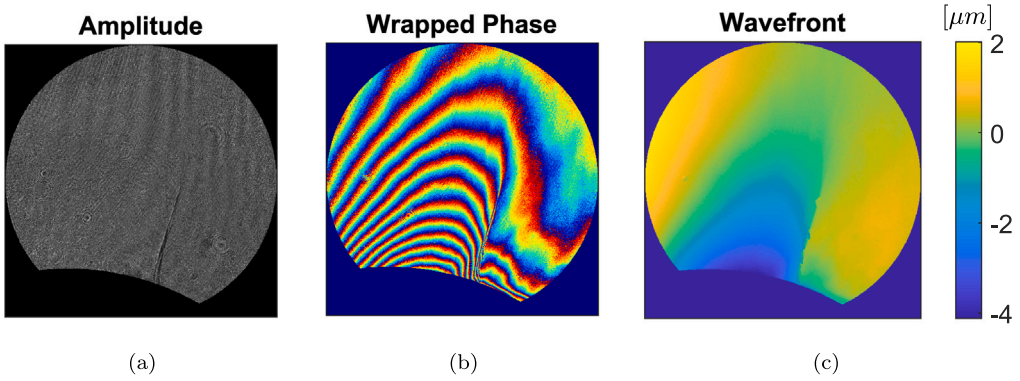

(a) (b) (c)

Fig. 4. (a) Amplitude of the beam. (b) The wrapped phase of the signal beam. (c) The reconstructed wavefront (unwrapped phase) with tip/tilt and piston removed.

beam using BC3. Tip/tilt of the reference beam is adjusted using the mirror right before BC3.

The Shack–Hartmann irradiance pattern was captured using a Phantom v1611 high-speed camera with a resolution of 768 × 768 pixels and a pixel width of 28 μm. The camera was equipped with a microlenslet array where each lenslet has a square 0.3 × 0.3 mm aperture with a focal length of 38.2 mm. This will provide an image that is divided into an array of sub-apertures or AOIs, each approximately 11 × 11 pixels. This results in a wavefront measurement with a resolution of roughly 71 × 71. Digital holography holograms were captured using a Phantom v1840 high-speed camera at full resolution of 2048 × 1944 pixels with a pixel width of 13.5 μm. The processed DH wavefront had a resolution of 511 × 511. Both cameras were synchronized to ensure that they capture the same instantaneous flow field. Multiple simultaneous wavefronts were collected with a sampling rate of 2.4 kHz. The exposure times were 1 microsecond for the Shack–Hartmann camera and 10 microseconds for the digital holography camera, both of which were sufficiently short to freeze the flow.

The cylinder geometry causes only a small region of the flow field to accelerate to be supersonic which is terminated by a local shock that is about 25–100 mm long, visible in Figs. 1(a) and 1(b). The small shock in this flow field is beneficial for this study as it only extends part of the way through the beam aperture. For the SHWFS this means we can crop out the dots contaminated by the shock effects while still having a continuous wavefront that spans around the local shock, which is important for the following discussion. With the DHWFS, there is a path of gradual increase in phase around the top of the shock, which allows us to correctly unwrap the phase, even if there is a very sharp phase gradient at the base of the shock. This setup is also beneficial because the shock decreases in strength further from the cylinder, which allows us to study a variety of shock strengths in a single measurement. As shock-related discontinuities will affect the reconstructed wavefront differently for these sensors, by comparing the wavefronts we can address the effects of the local discontinuities on the wavefront reconstruction algorithms.

While the authors could not find work explicitly studying the effects of shocks on digital holography measurements, it has been used to measure and remove phase aberrations from shocks to get higher-quality images of explosion fragments in [48] which suggests that they were able to measure the correct phase fairly accurately. There is also a great deal of literature studying digital holography 3D imaging of discontinuous objects [49–51] which suggests that the discontinuity does not degrade the accuracy of the measurement other than making it difficult to unwrap. However, since our setup has a shock extending only partially through the aperture, we can unwrap around the top of the shock easily. We performed additional wave-optics simulations of a case more similar to our setup and found the shock should have very little effect on the digital holography measurement, so we felt it appropriate to assume the digital holography measured wavefront represented the “ground truth”.

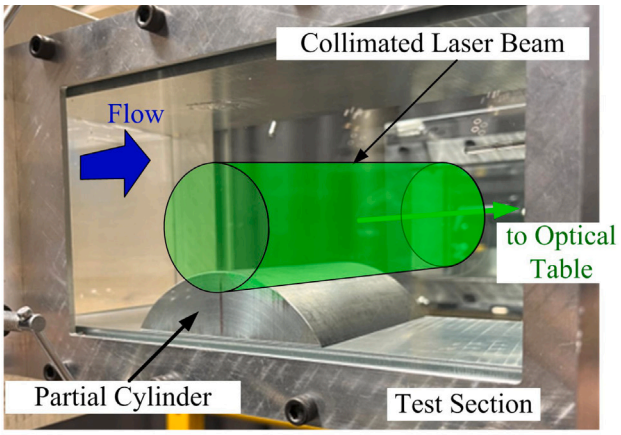

(a)

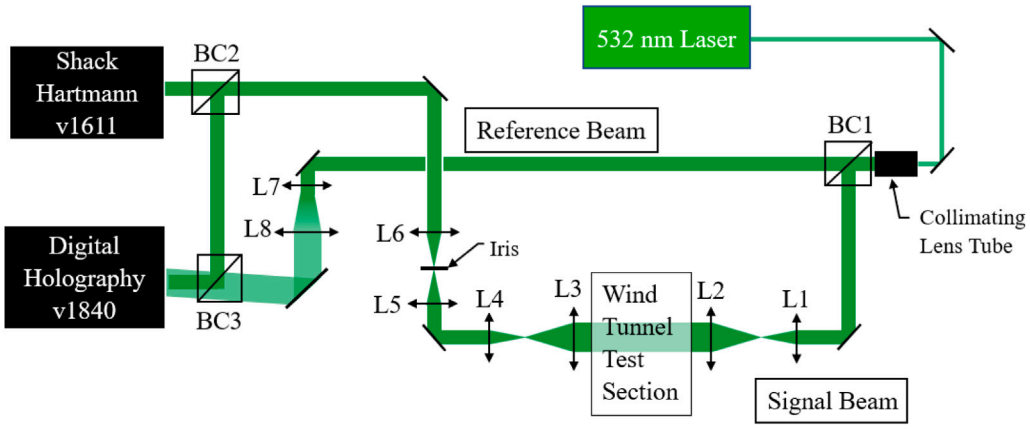

(b)

Fig. 5. (a) Tunnel test section with the mounted 2-D partial cylinder and the spanwise collimated laser beam. (b) Schematics of the experimental optical layout with both SHWFS and DHWFS.

4. Results

4.1. SHWFS–DHWFS comparison

In order to compare the wavefront calculated from SHWFS and DHWFS, a few steps of preprocessing were required. As mentioned in Section 2.2, we first filtered out poor quality frames that had trouble unwrapping the phase and excluded them from analysis.

Due to the different sensor sizes of the cameras (DHWFS: 27.6 × 26.2 mm) (SHWFS: 35.8 × 22.4 mm), the images captured on the cameras do not have the same area. Thus alignment of the cameras is needed to properly compare between the DHWFS and SHWFS. An iris was placed in the beam train to cut the beam down to about 10 mm to ensure that the beam is within the aperture of both cameras. This provided a distinct shape with a known size which allowed us to ensure that the wavefronts were scaled correctly between the sensors. A registration image was taken with both sensors with the wind tunnel off and we then downsampled the DHWFS data from 511 × 511 pixels to 71 × 71 pixels to match the much lower resolution of the SHWFS through bicubic interpolation with the *imresize* MATLAB function. Using cross-correlation, we adjusted the position of the SHWFS and DHWFS images until the cross-correlation reached a maximum. This indicates that the two relative positions of the two images are now aligned.

After alignment, a common mask was applied to both wavefronts to ensure they contained signal in the same regions which was important because next, tip/tilt and piston components of the wavefront were removed from both wavefronts. At this point, the wavefronts from the two sensors could be directly compared on a pixel-to-pixel basis. The difference between the two wavefronts measured by the SHWFS and the DHWFS was taken to get the difference map $\Delta_W = W_{SH} - W_{DH}$. This process is shown in Fig. 6.

Example wavefronts, simultaneously measured by SHWFS and DHWFS, are shown in Figs. 7(a) and 7(b), respectively. The wavefronts look similar, however, when we take a slice across the shock along the lines in Figs. 7(a) and 7(b), which are shown in Fig. 7(c), it is clear that the SHWFS is underestimating the phase jump induced by the shock. As it will be shown later, some dots in the Shack–Hartmann image are distorted, which results in a measured C-tilt is much smaller than the large wavefront tilt that exists at that point of the wavefront. This leads to a much flatter reconstructed wavefront. The temporal mean of the spatial rms of the DH wavefront was 0.61 μm while only 0.28 μm for the SH wavefront. This shows that the SHWFS is underestimating the phase jump as expected. It is interesting that in this case, the Shack–Hartmann reconstructed wavefront increases by around 4λ across the shock, where the analysis in Refs. [22] and [28] showed that the SHWFS should only be able to resolve a jump in the wavefront of $\lambda/2$. There are a few factors that we believe allow this to occur.

First of all, our shock only extends part of the way through that aperture, which allows us to reconstruct the wavefront around the shock, and by following the slopes along this path, you end up with a value much larger value than $\lambda/2$. To test this, the same Shack–Hartmann wavefront shown in Fig. 7(a) was reconstructed using a

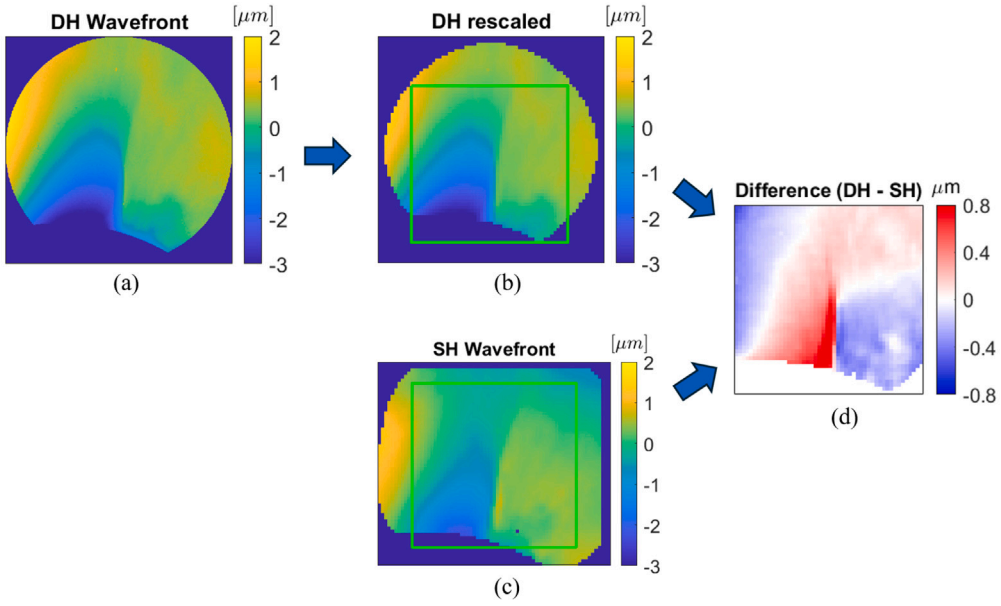

Fig. 6. The SHWFS and DHWFS comparison process. The DH wavefront, (a), is descaled to match the SH resolution. The green boxes over the DH, subplot (b), and SH, subplot (c), wavefronts show the areas where the SH and DH are aligned. These areas are cropped out and a difference map, (d), is computed.

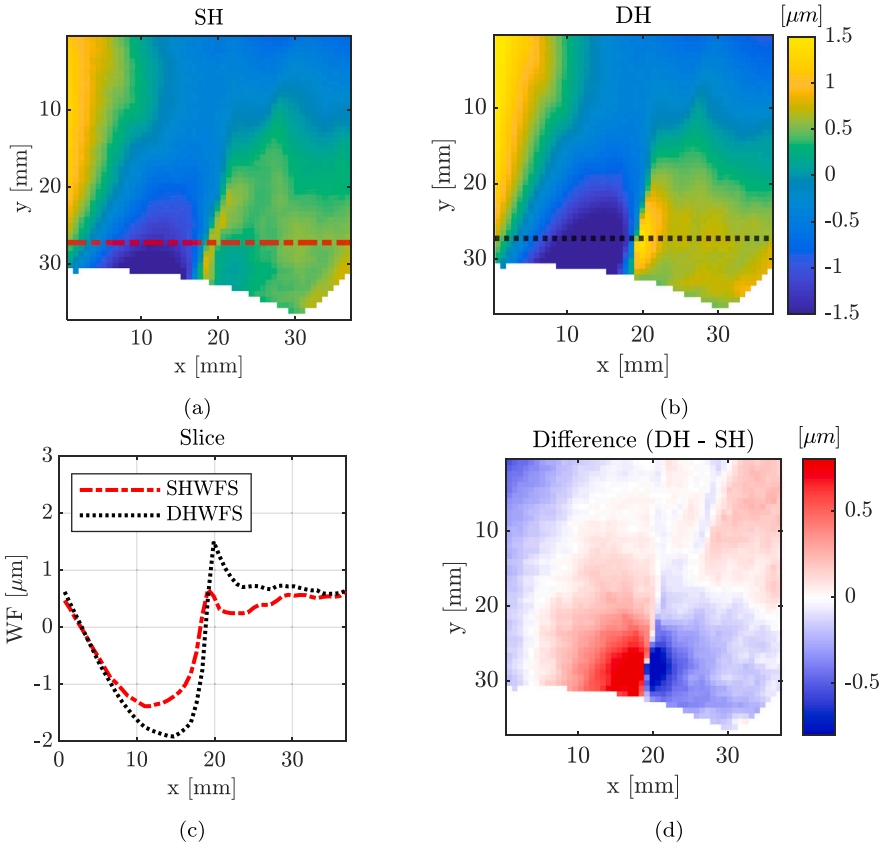

Fig. 7. The reconstructed wavefront for (a) the SHWFS and (b) DHWFS. The colorbar is shared for both SHWFS and DHWFS. (c) The cross-sectional slice of Figs. 7(a), 7(b) at the lines drawn on the figures. (d) The difference between the SHWFS and DHWFS. Colormaps in all plots show the wavefront in microns.

smaller portion of the aperture, such that the shock went through the entire aperture, ensuring a large increase in the wavefront would not be found due to the wavefront reconstructing around the shock. Even in this case, the reconstructed wavefront increased by about 3λ. This large jump could be possible because the shock is not perfectly on-axis with the beam propagation direction. Ref. [22] analyzed how a SHWFS will perform for a ramp function wavefront for the case of a shock at an angle, finding that it could produce more complicated irradiance patterns other than the bifurcated dot produced by a discontinuous phase. The interaction with the wall boundary layer makes shocks generally unsteady, especially the transonic shock in our experiment which shifts on the order of a centimeter upstream and downstream in time. Similar

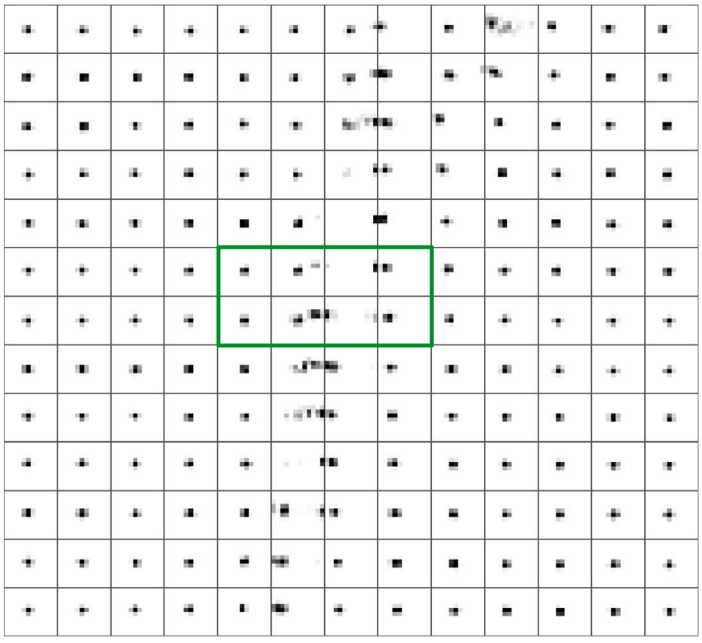

(a)

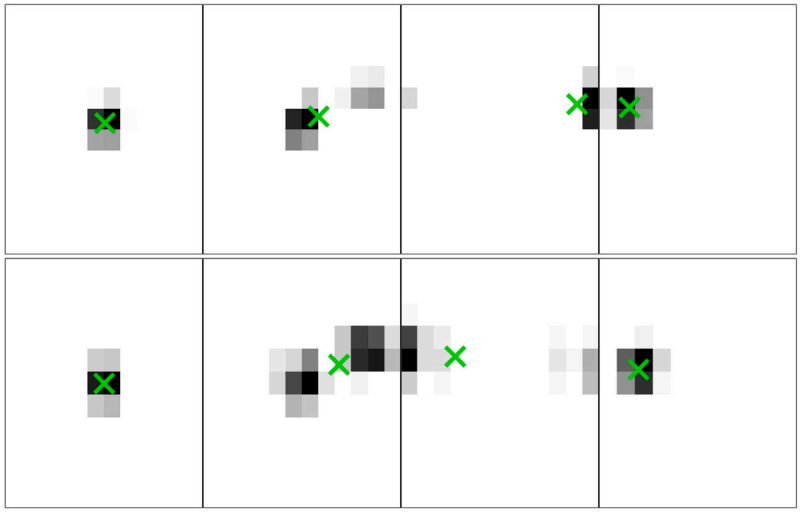

(b)

Fig. 8. (a) An intensity-inverted SHWFS dot pattern showing most dots are well defined, diffraction limited dots while a few distorted dots are caused by the supersonic shock. (b) are magnified images showing the splitting dots and the green "x" show where the centroid is calculated to be.

to a shock at an angle, this would result in a wavefront that follows some ramp or other function increase across some distance, rather than following the instantaneous step function increase of an idealized shock which would result in a more complex irradiance pattern instead of a simple bifurcation. In our data, we observed irradiance patterns with multiple peaks, smearing, or large displacements, as illustrated as intensity-inverted image in Fig. 8(a). Fig. 8(b) highlights cases where dots spread significantly or shift into neighboring AOIs. The calculated centroid locations in Fig. 8(b) are marked by a green "x", and we can see how some of these irradiance patterns can create large tilt estimates. Further work is needed to refine this analysis and better understand the relationship between the measured far-field data and the actual wavefront slope across the shock region.

The spatial map of the wavefront difference, Δ_W, is shown in Fig. 7(d) where we can see how the SHWFS's underestimation of the slope at the shock causes the error to bleed out well beyond the shock due to the global nature of least square reconstruction. A convenient single number metric for grading the performance of the SHWFS compared to the ground truth DHWFS is to take the spatially-averaged standard deviation of the difference, $\Delta_{W,rms} = \langle \Delta_W(x,y,t)^2 \rangle_{(x,y)}$. This is equivalent to the L2 error norm of the SHWFS measurement. We can extend this thought by looking at these results in the farfield. When we apply the phase measured by the DHWFS to a complex optical field and propagate it to the farfield, as you expect, the beam has significant spreading due to the strong distortion which you can see in Fig. 9(a). If we apply the phase difference between the sensor measurements and propagate, to simulate a beam corrected by an AO system using a SHWFS, we see in Fig. 9(b) that we do get improvement, but the farfield irradiance is still far from diffraction limited. The colormap in these images shows the farfield irradiance normalized by the maximum diffraction limited irradiance.

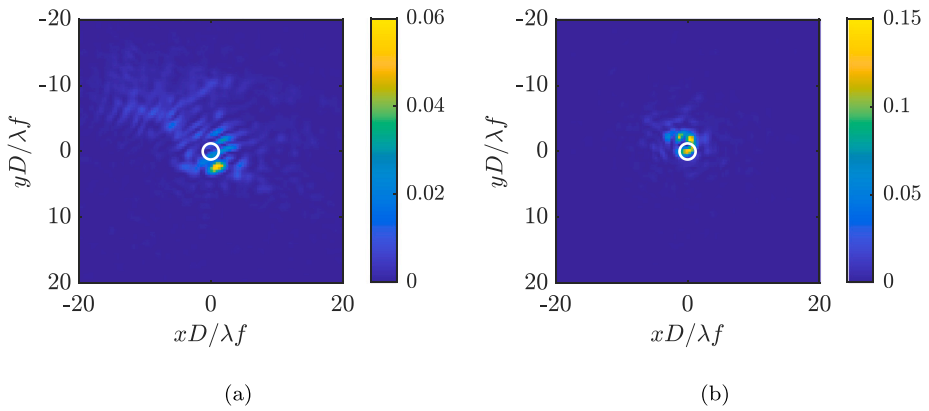

Fig. 9. (a) Irradiance of DH measured wavefront projected to the farfield. (b) Farfield irradiance resulting from the difference in wavefront between DH and SH. White circle outlines the Airy disk. Irradiances normalized by maximum diffraction limited irradiance.

Measurements were taken at varying Mach numbers and the unsteady nature of the transonic shock creates even more variation in the shock strength between frames. In order to see how the Shack–Hartmann performance changes with shock strength, the $\Delta_{W,rms}$ metric was computed for every frame and across the different tunnel runs. The peak-to-valley height of the digital holography wavefront was used to quantify the shock strength. Fig. 10(a) shows $\Delta_{W,rms}$ as a function of the peak to valley height, where $\Delta_{W,rms}$ has been averaged within peak to valley height bins of width 0.2 μm, with values ranging from 2–4.5 μm. One standard deviation from the mean values is shown by the shaded region. We can see how the SHWFS measurement error increases with shock strength and appears to grow nonlinearly. While the cases with the lowest DH peak to valley were fully subsonic with no shock, the rms of the residual does not go to zero. This residual error is likely due to a slight misalignment between the sensor wavefronts, and other differences that come from these two sensors handling system imperfections differently which exist even when there are no shocks.

To measure performance in the farfield, Δ_W was converted to a complex optical field and propagated. The normalized power in a diffraction-limited bucket, $nPIB_{DL}$, was then calculated. This value was normalized by dividing the power in this bucket by the total power in the aperture. This is plotted against the peak-to-valley height in Fig. 10(b). Here we see the power in the bucket decreases nonlinearly with shock strength down to the lowest value of around 30% power in the bucket for the strongest shock case. Again the performance for the subsonic cases was still lower than diffraction-limited PIB likely due to slight misalignment between the sensors and SHWFS reconstruction error.

4.2. Shack–Hartmann statistical analysis

A key step in the shock-tolerant wavefront reconstruction algorithm introduced by Defoor [28] is to find shock-affected AOIs in the Shack–Hartmann and remove them. In this work, we study different parameters and their ability to identify these AOIs with distorted, non-diffraction-limited dots.

The three methods tested are standard deviation, kurtosis, and slope discrepancy. The normalized standard deviation, σ_{Norm}, and normalized kurtosis, $Kurt_{norm}$, were calculated for each AOI using Eqs. (5) and (8) respectively which are shown in Figs. 11(a) and 11(b). The slope discrepancy field was computed with Eq. (10). The algorithm to calculate the higher-order statistics (standard deviation, skewness, and kurtosis) takes Matlab an average of 300 ms for one frame of the Shack–Hartmann. For reference, it takes Matlab an average of 25 ms to calculate the centroids. This was performed on a laptop with a 12-core Intel i7-1260p.

All of the maps clearly show the shock location in the center of the frame extending away from the cylinder surface. The standard deviation and kurtosis maps seem to identify the same AOI's for the shock while the slope discrepancy selects a larger region around the shock. When visually inspecting the dots highlighted by the different methods, the statistics based methods seem to correctly highlight the distorted dots, while slope discrepancy has a high value even for AOI's with dots that appear diffraction-limited. This is due to the least squares reconstructor spreading error out, as we saw when comparing wavefronts. The incorrect slope measurement at the shock pulls the wavefront reconstruction away from the truth, which increases error and slope discrepancy nearby. The statistics based methods have some noise around the perimeter of the aperture, which does not show up in the slope discrepancy. This noise is worse in the standard deviation than in the kurtosis.

4.2.1. Masking and reconstruction

Using either the standard deviation, kurtosis, or slope discrepancy we can set a prescribed threshold and mask out AOIs with values larger than the threshold. These poor-quality slope measurements are then excluded from the wavefront reconstruction. The resulting wavefront was compared to properly-masked DHWFS wavefronts as before and the maps of the difference between the two wavefronts, Δ_W, are shown in Fig. 13(a), 13(b), and 13(c) for wavefronts reconstructed with masks created using σ_{Norm}, $Kurt_{Norm}$, and δ respectively. In these figures, Δ_W is shown for wavefronts constructed using increasingly aggressive masks, which use smaller threshold values. The plot titles show what percentage of the total points in the wavefront were masked out. First looking at the standard deviation mask case in Fig. 13(a), we see Δ_W improves as we make the mask larger, shrinking the red region in front and the blue region behind the shock. The kurtosis difference maps in Fig. 13(b) are very similar to the standard deviation maps. This is expected as both capture similar distortions of the intensity in the AOIs. In both cases, we see that for very aggressive thresholds, the magnitude of Δ_W decreases significantly but never goes to zero everywhere. There still remains significant error just upstream of the shock. Both methods also mask out a bit of noise around the outside edges which is more clear in the more aggressive masks. This is traced back to some slight aberrations in the test setup that shift the image plane on the outer dots. This blurs the dots and creates a wider intensity distribution that both standard deviation and kurtosis pick up on, but is worse for standard deviation.

The slope discrepancy maps of Δ_W in Fig. 13(c) show that the slope discrepancy based mask also helps reduce wavefront error. The magnitude of Δ_W also does not go to zero everywhere here either, however, in this case, the residual error is downstream of the shock. We also do not see the noise artifacts that were in the standard deviation and kurtosis masks since slope discrepancy is less susceptible to these types of system aberrations and is looking at the difference in slope rather than the intensity distribution in the AOI. Instead, for very low

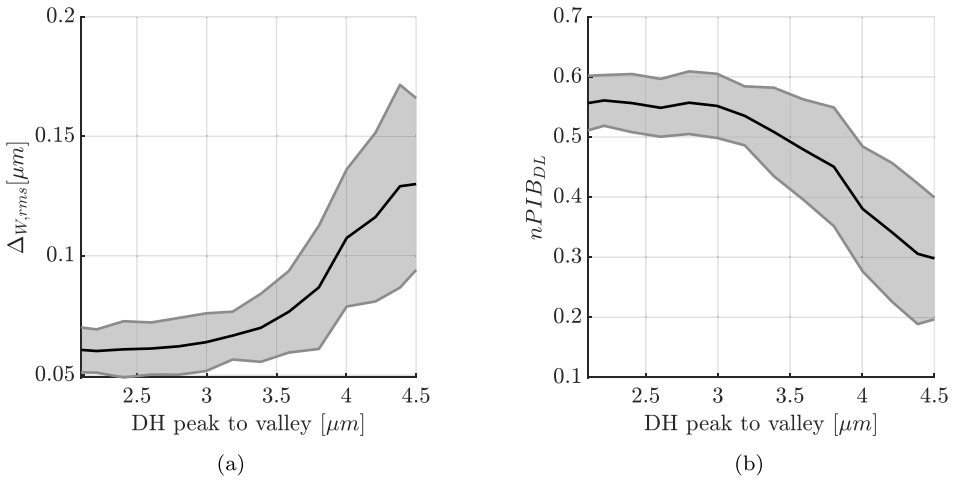

Fig. 10. Time averaged (a) rms of the Δ_W wavefront and (b) $nPIB_{DL}$ of the Δ_W wavefront propagated to the farfield as a function of the peak to valley height of the digital holography measured wavefront. The shaded region represents plus or minus one standard deviation.

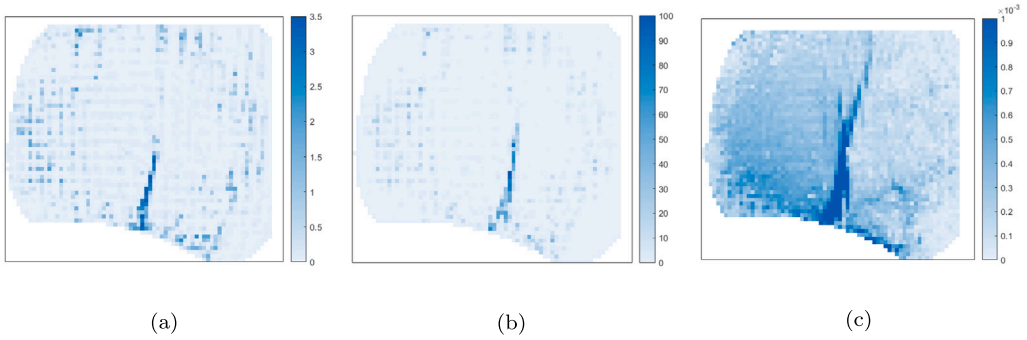

Fig. 11. Maps showing the values of (a) standard deviation, (b) kurtosis, and (c) slope discrepancy. The darker the AOI, the higher the value. Setting a threshold creates a mask that eliminates the AOIs that exceed that threshold.

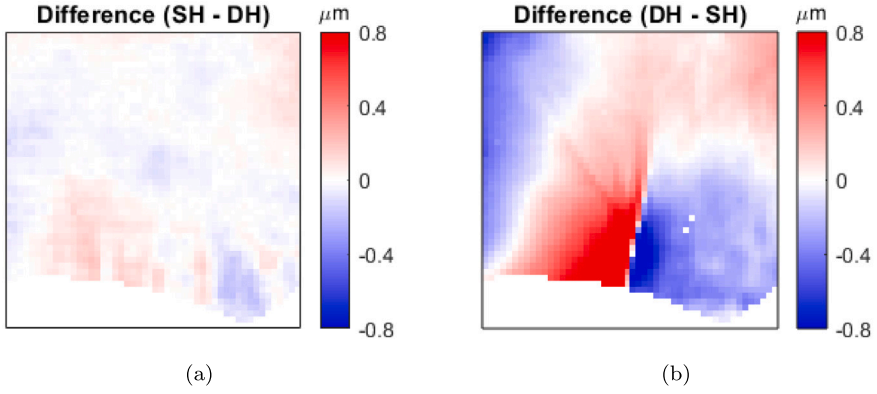

Fig. 12. The difference maps comparing (a) subsonic flow and (b) supersonic flow. In subsonic flow, the RMS values is 0.10 while the supersonic flow has an RMS value of 0.24. Units are in μm.

slope discrepancy thresholds, a large chunk on the bottom left of the wavefront gets excluded from reconstruction.

A note here is that reconstruction was performed before cropping out the window for comparison. For the Southwell reconstruction process to work, the sparse matrix must be continuous. In Fig. 11, the masks with more aggressive thresholds have isolated points that are not interconnected. This is caused by the windowing operation which crops out the connecting points, creating an apparent discontinuity between the points. Fig. 6 shows the area that is cropped out of the wavefronts. Thus even though the comparison maps may suggest isolated points, the complete SH wavefront remains continuous before cropping.

As before, $\Delta_{W,rms}$ was calculated to give a single metric for the frame which we could use to compare many different frames. This makes it easier to identify large differences in the comparison map. As shown in Section 4.1, $\Delta_{W,rms}$ increases when there is a shock in the flow. Fig. 12(a) shows the difference map between the subsonic and supersonic case. The subsonic case has an $\Delta_{W,rms}$ of roughly 0.06 μm and the supersonic case has an $\Delta_{W,rms}$ of about 0.24 μm. Fig. 14 shows $\Delta_{W,rms}$ as a function of the mean percentage of points excluded from the reconstruction, which allows us to compare the efficiency of each algorithm. In this plot the $\Delta_{W,rms}$ for the case when no mask is used is shown with the dashed black line. The cyan dashed line is the average $\Delta_{W,rms}$ for

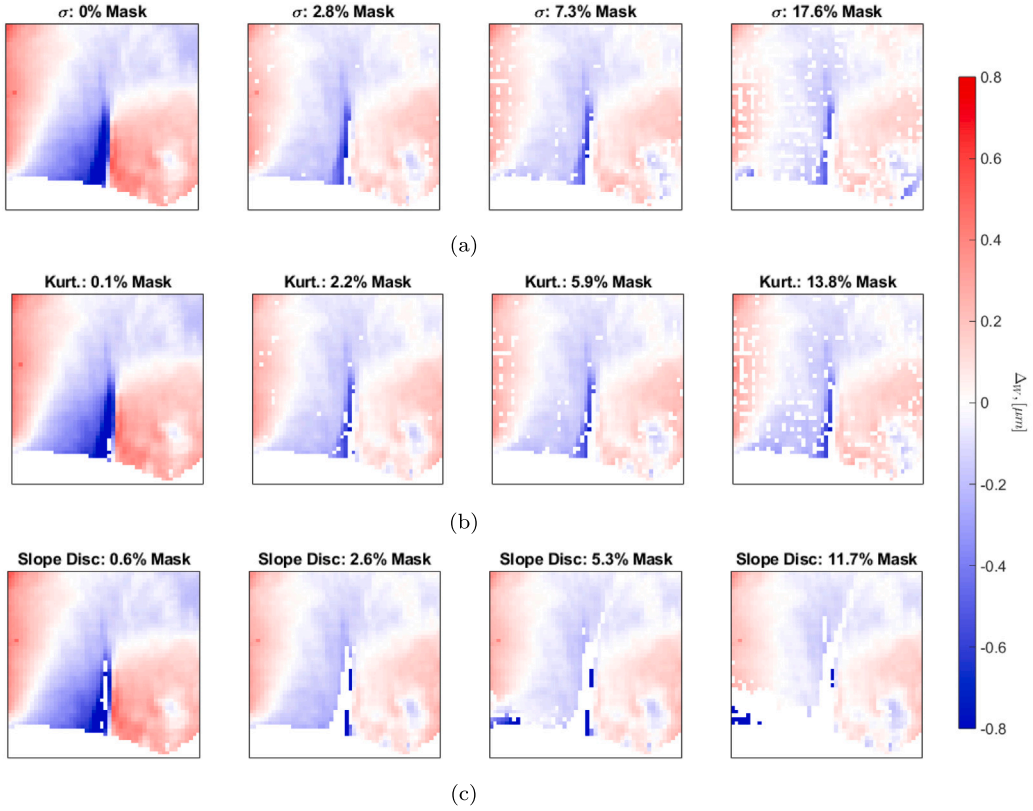

Fig. 13. Selected difference maps showing how masks change for (a) standard deviation, (b) kurtosis, and (c) slope discrepancy.

the subsonic cases that have no shock, which provides a lower bound on performance. The standard deviation and kurtosis masks both see quick improvements in $\Delta_{W,rms}$ as more points are removed up to the point when the masks remove roughly 2% of the AOIs, where kurtosis begins to see slight improvement. Slope discrepancy has a similar, but slightly worse performance than the statistics. After the 2% point, all methods begin to see less improvement as more points are excluded from reconstruction. This likely means that these algorithms start to remove more points which were not actually degrading reconstruction performance. This can be seen in all the of points getting masked out in Fig. 13 that are far from the shock. For the slope discrepancy mask, however, the $\Delta_{W,rms}$ actually gets worse if the slope discrepancy threshold is too aggressive. We also see that the $\Delta_{W,rms}$ of the different masks does not reach the cyan line of the subsonic case, even for very small thresholds. As previously pointed out, Fig. 14 shows there is still some noticeable difference in the wavefronts which have aggressive masks applied, especially near the front of the shock (in darker blue).

The thresholds for each of these methods used in the rest of the analysis were chosen by visual inspection. From Fig. 14, a mask of about 2.4% is a good balance between points removed and an improved $\Delta_{W,rms}$ value. For reference, a non-distorted dot would have normalized σ and $Kurt$ around zero, but the thresholds used here removed points with σ and $Kurt$ values of 2 and 50 or higher, respectively. However, the key thing to note here is this mask is not universal. Different masks will need to be created for each frame if the shock is unsteady and the size and position of the region affected by the shock change in time.

4.2.2. Interpolation

Once points are removed using these masks, the missing information must be filled in. After reconstruction, spline interpolation was used to mimic fitting the wavefront to a continuous surface deformable mirror. The SH wavefronts interpolated from the standard deviation, kurtosis, and slope discrepancy masked wavefronts were compared to the DH wavefront, and their $\Delta_{W,rms}$ maps are shown in Figs. 15(a), 15(b), and 15(c), respectively. Majority of the dark red and blue regions, indicating large differences are mostly gone compared to the original difference map.

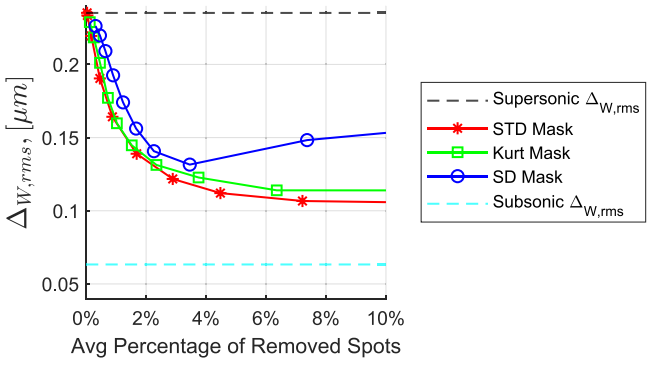

Fig. 14. Spatial rms of the difference between the SH and DH wavefronts as a function of how many points are excluded from SH reconstruction. Black dashed line shows $\Delta_{W,rms}$ when no points are removed. Cyan dashed line shows $\Delta_{W,rms}$ for a subsonic case which has no shock.

Again, $\Delta_{W,rms}$ was plotted in Fig. 16 as a function of percentage of points excluded from reconstruction. The standard deviation and kurtosis based masks again see the same improvement in performance for each point removed up to around 2% of the total points. After this, the standard deviation masking performs slightly better than kurtosis, however, $\Delta_{W,rms}$ asymptotes at 0.16 μm which is much larger than $\Delta_{W,rms}$ = 0.06 μm for the subsonic case and larger than the best performance ($\Delta_{W,rms}$ = 0.1 μm) we saw in Fig. 14. For the first 1% of total points removed, slope discrepancy has a worse $\Delta_{W,rms}$ than the statistics-based methods, but it continues to decrease when the statistics-based methods level off allowing it to reach a lower error.

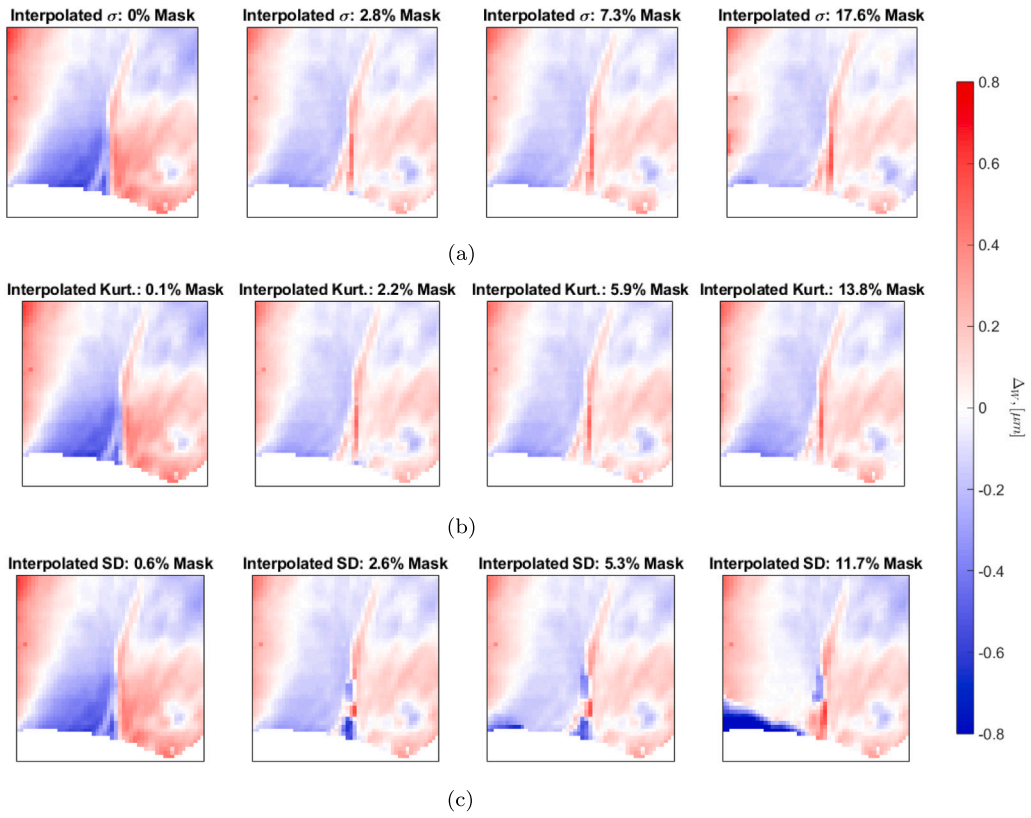

Fig. 15. The difference maps using SH wavefront interpolated from the masks (a) standard deviation, (b) kurtosis, and (c) slope discrepancy masks.

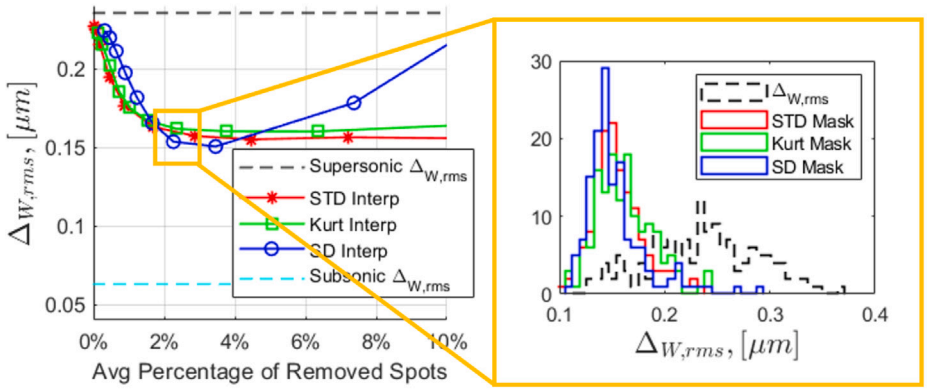

Fig. 16. Using the masks as shown in Fig. 14, the interpolated wavefronts are shown to also improve using these masks. Taking the maps with around 2.4% masks, the frames for these sets can be expanded into a histogram. The slope discrepancy distribution shows a general improvement of the $\Delta_{W,rms}$ over the higher order statistic distribution.

However, the error is still much larger $\Delta_{W,rms}$ than the subsonic case. Masking out the shock, where $\Delta_{W,rms}$ is going to tend to be large, naturally decreases the $\Delta_{W,rms}$. Thus if plotting the $\Delta_{W,rms}$ of just the masked wavefront without reconstruction, a linear relationship between the percentage removed and the $\Delta_{W,rms}$ is observed. Interpolating adds back the missing points, however, it is not perfect thus differences in the map remain. This naturally increases the $\Delta_{W,rms}$.

The key takeaway is that between the masks and interpolation maps, all three masking methods, standard deviation, kurtosis, and slope discrepancy had relatively similar $\Delta_{W,rms}$ profile. This indicates that these three techniques performed relatively similarly in capturing the AOIs affected by the shock. After interpolating, slope discrepancy has a slightly lower $\Delta_{W,rms}$ than the statistical methods. This would suggest that slope discrepancy eliminates the points most affected by the smoothing of the least-squares reconstruction more than the statistics. Fig. 16 also expands those the 2.4% mask into a histogram points over 200 frames. The histogram also shows that there are still outliers with all three methods but in general most frames have a smaller $\Delta_{W,rms}$ over the original distribution as shown in the dotted black line. This also shows that the slope discrepancy is shifted a little more left than the statistic methods.

5. Conclusion

Wavefront sensors, particularly the Shack–Hartmann wavefront sensor (SHWFS) and the digital holography wavefront sensor (DHWFS), are crucial in the development of directed energy systems, especially for airborne platforms. Although both are widely used for accurate wavefront sensing, SHWFS faces challenges in correctly measuring wavefronts in optical environments with steep density gradients associated with shocks. To investigate this limitation in SHWFS, a series of experiments were conducted in a transonic flow wind tunnel, where

a localized shock was created over a partial cylinder. A collimated laser beam was passed along the local shock creating a large gradient in the wavefronts. The resulting wavefronts were simultaneously measured by both SHWFS and DHWFS, treating DHWFS as the "ground truth". Direct comparisons of SHWFS and DHWFS wavefronts showed that SHWFS, with a standard Southwell reconstruction algorithm, significantly underestimated wavefront jumps across the shock due to incorrect estimates of the wavefront slopes.

To address these inaccuracies, a modification of the Southwell wavefront reconstruction algorithm was developed, aiming to detect and correct shock-affected areas in SHWFS images. Three methods were evaluated in their effectiveness at identifying shock-distorted dots: standard deviation, kurtosis, and slope discrepancy. While all methods performed similarly in identifying the distorted dots, slope discrepancy proved slightly more effective overall. It was demonstrated that by excluding shock-affected areas, recomputing the wavefront in the remaining region, and spline interpolating the excluded region, the reconstruction accuracy of SHWFS is significantly improved. While slope discrepancy yielded lower errors than standard deviation and kurtosis, it could not eliminate all shock-affected errors. A small error in the location of the sharp gradient within the interpolated region of the reconstructed wavefront led to significant wavefront error.

Overall, these findings contribute to the advancement of shock-wave-tolerant phase reconstruction algorithms for the SHWFS and introduce a novel reconstruction algorithm that reduces the root mean squared error of SHWFS wavefronts by approximately 30%. However, further research is necessary to refine the correction of shock-affected points, especially in cases where the shock extends through the entire aperture.

CRediT authorship contribution statement

Ethan D. Chu: Writing – review & editing, Writing – original draft, Visualization, Investigation, Formal analysis. **Timothy J. Bukowski:** Writing – review & editing, Visualization, Investigation, Formal analysis. **Stanislav Gordeyev:** Writing – review & editing, Supervision, Funding acquisition, Conceptualization.

Declaration of competing interest

The authors declare that they have no known competing financial interests or personal relationships that could have appeared to influence the work reported in this paper.

Acknowledgments

The authors would like to thank Matt Kalensky for discussions that have been extremely helpful in this work. The authors thank Zareb Noel and Mark Rennie for helping to develop the digital holography system and related processing codes. We also thank Matthew Kemnetz for his comments and insight, especially in regards to the experimental setup.

This work was partially funded by the Department of Aerospace and Mechanical Engineering at the University of Notre Dame and partially supported by the Office of Naval Research, United States, Grant number N00014-22-1-2454.

Data availability

The authors do not have permission to share data.

References

[1] B.C. Platt, R. Shack, History and principles of shack-hartmann wavefront sensing, J. Refract. Surg. 17 (5) (2001) S573–S577.
[2] T. Kohnen, D.D. Koch, Cataract and Refractive Surgery, Springer Science & Business Media, 2006.
[3] D.R. Neal, J. Mansell, Application of shack-hartmann wavefront sensors to optical system calibration and alignment, Adapt. Opt. Ind. Med. (1999) 234–240.
[4] J. Wang, X. Wang, L. Peng, J. Wang, Z. Liu, L. Li, M. Cai, B. Liu, W. Li, X. Zhang, Method for testing freeform surfaces based on a shack-hartmann sensor with plane wavefront scanning and stitching, Opt. Expr. 31 (22) (2023) 36702–36724, http://dx.doi.org/10.1364/OE.503494.
[5] G.-H. Go, D. gu Lee, J. Oh, G. Song, D. Lee, M. Jang, Meta shack–hartmann wavefront sensor with large sampling density and large angular field of view: phase imaging of complex objects, Light: Sci. Appl. 13 (2024).
[6] X. Tao, Z. Dean, C. Chien, O. Azucena, D. Bodington, J. Kubby, Shack-hartmann wavefront sensing using interferometric focusing of light onto guide-stars, Opt. Expr. 21 (25) (2013) 31282–31292, http://dx.doi.org/10.1364/OE.21.031282.
[7] M.T. Banet, M.F. Spencer, Compensated-beacon adaptive optics using least-squares phase reconstruction, Opt. Expr. 28 (24) (2020) 36902–36914, http://dx.doi.org/10.1364/OE.409134.
[8] I. Galaktionov, A. Nikitin, J. Sheldakova, V. Toporovsky, A. Kudryashov, Focusing of a laser beam passed through a moderately scattering medium using phase-only spatial light modulator, Photonics 9 (5) (2022) http://dx.doi.org/10.3390/photonics9050296, URL https://www.mdpi.com/2304-6732/9/5/296.
[9] J.D. Barchers, D.L. Fried, D.J. Link, Evaluation of the performance of hartmann sensors in strong scintillation, Appl. Opt. 41 (6) (2002) 1012–1021.
[10] G. Rousset, Wave-Front Sensors, Cambridge University Press, 1999.
[11] R.K. Tyson, Introduction To Adaptive Optics, SPIE, 2000, http://dx.doi.org/10.1117/3.358220.
[12] P. Merritt, M. Spencer, Beam Control for Laser Systems, The Directed Energy Professional Society, 2018.
[13] J.M. Sontag, M.R. Kemnetz, S. Gordeyev, Spanwise wavefront analysis of turbulence amplification in a turbulent boundary layer forced by an external shear layer, in: AIAA Scitech 2019 Forum, American Institute of Aeronautics and Astronautics, 2019, http://dx.doi.org/10.2514/6.2019-0054.
[14] J. Wells, M. Kalensky, R.M. Rennie, E.J. Jumper, Experimental and computational investigation of shack–hartmann wavefront sensor measurements through a free shear layer, Opt. Eng. 63 (01) (2024) http://dx.doi.org/10.1117/1.oe.63.1.014108.
[15] J. Sontag, S. Gordeyev, Optical diagnostics of spanwise-uniform flows, AIAA J. 60 (9) (2022) 5031–5045, http://dx.doi.org/10.2514/1.j061692.
[16] S. Gordeyev, E. Jumper, M. Whiteley, Aero-optical effects: Physics, analysis and mitigation, in: Wiley Series in Pure and Applied Optics, Wiley, 2023.
[17] S. Gordeyev, E. Jumper, Fluid dynamics and aero-optics of turrets, Prog. Aerosp. Sci. 46 (8) (2010) 388–400.
[18] D.T. Kyrazis, Airborne Laser Laboratory departure from Kirtland Air Force Base and a brief history of aero-optics, Opt. Eng., Bellingham 52 (7) (2012) 1–6.
[19] E.J. Jumper, M.A. Zenk, S.V. Gordeyev, D.A. Cavalieri, M. Whitely, Airborne Aero-Optics Laboratory, Opt. Eng., Bellingham 52 (7) (2013) 1–12.
[20] T.J. Bukowski, S. Gordeyev, M. Kalensky, M.R. Kemnetz, Study of unsteady surface flowfields on and around turrets with different protrusions, AIAA J. 61 (12) (2023) 5320–5331.
[21] M. Kalensky, M.R. Kemnetz, M.F. Spencer, Effects of shock-related discontinuities on SHWFS measurements: modeling and simulation, in: J.J. Dolne, M.F. Spencer (Eds.), Unconventional Imaging and Adaptive Optics 2022 12239, International Society for Optics and Photonics, SPIE, 2022, 122390J.
[22] M. Kalensky, M.R. Kemnetz, M.F. Spencer, Effects of shock waves on shack–hartmann wavefront sensor data, AIAA J. 61 (6) (2023) 2356–2368.
[23] J. Panda, G. Adamovsky, Laser light scattering by shock waves, Phys. Fluids 7 (9) (1995) 2271–2279.
[24] M.R. Kemnetz, M. Kalensky, T.E. DeFoor, M.F. Spencer, Experimental investigation into the effects of shock waves on shack-hartmann wavefront sensor measurements, in: J.J. Dolne, M.F. Spencer, S.R. Bose-Pillai (Eds.), Unconventional Imaging, Sensing, and Adaptive Optics 2023 12693, International Society for Optics and Photonics, SPIE, 2023, 1269314.
[25] F. Feng, C. Liang, D. Chen, K. Du, R. Yang, C. Lu, S. Chen, W. He, P. Xu, L. Chen, L. Tao, H. Mao, Moment-based space-variant shack–hartmann wavefront reconstruction, Opt. Commun. 540 (2023) 129515.
[26] M. Kalensky, Branch-point identification using second-moment shack–hartmann wavefront sensor statistics, Appl. Opt. 62 (23) (2023) G101.
[27] M. Kemnetz, M. Kalensky, A. Roeder, Z. Noel, Effects of shock-related discontinuities on SHWFS measurements: experimental results (conference presentation), in: J.J. Dolne, M.F. Spencer (Eds.), Unconventional Imaging and Adaptive Optics 2022 12239, International Society for Optics and Photonics, SPIE, 2022, 122390I.
[28] T.E. DeFoor, M. Kalensky, M.R. Kemnetz, T.J. Bukowski, M.F. Spencer, Shock-wave tolerant phase reconstruction algorithm for shack–hartmann wavefront sensor data, Opt. Eng., Bellingham 62 (12) (2023) 123103.

[29] T.E. DeFoor, T.J. Bukowski, M. Kalensky, S. Gordeyev, Phase discontinuity classification from single-aperture irradiance patterns using machine learning, in: J.J. Dolne, S.R. Bose-Pillai, M. Kalensky (Eds.), Unconventional Imaging, Sensing, and Adaptive Optics 2024 13149, International Society for Optics and Photonics, SPIE, 2024, 131490F, http://dx.doi.org/10.1117/12.3028274.

[30] Z.A. Noel, M.R. Kemnetz, S. Gordeyev, R.M. Rennie, Robust, regularized wavefront reconstruction of shack-hartmann data in discontinuous flow, in: J.J. Dolne, M.F. Spencer, S.R. Bose-Pillai (Eds.), Unconventional Imaging, Sensing, and Adaptive Optics 2023 12693, International Society for Optics and Photonics, SPIE, 2023, 1269318.

[31] W. Yang, J. Wang, B. Wang, A method used to improve the dynamic range of shack–hartmann wavefront sensor in presence of large aberration, MDPI Sensors 22 (2022) 7120, http://dx.doi.org/10.3390/s22197120.

[32] S. Gordeyev, R. Burns, E. Jumper, S. Gogineni, M. Paul, D. Wittich, Aero-optical mitigation of shocks around turrets at transonic speeds using passive flow control, in: 51st AIAA Aerospace Sciences Meeting Including the New Horizons Forum and Aerospace Exposition, Grapevine, TX, AIAA Paper, 2013, 2013-0717.

[33] E.D. Chu, T.J. Bukowski, S. Gordeyev, Studies of local shock effects on shack-hartmann and digital holography wavefront sensors, in: J.J. Dolne, M.F. Spencer, S.R. Bose-Pillai (Eds.), Unconventional Imaging, Sensing, and Adaptive Optics 2023 12693, International Society for Optics and Photonics, SPIE, 2023, 1269317.

[34] W. Southwell, Wave-front estimation from wave-front slope measurements, J. Opt. Soc. Am. 70 (8) (1980) 998–1006.

[35] Thor Labs, Shack-hartmann wavefront dwg, 2023, (Online; accessed 28 July 2023).

[36] D.L. Fried, Least-square fitting a wave-front distortion estimate to an array of phase-difference measurements, J. Opt. Soc. Am. 67 (3) (1977) 370–375.

[37] R.H. Hudgin, Wave-front reconstruction for compensated imaging, J. Opt. Soc. Am. 67 (3) (1977) 375–378.

[38] A.M. Nightengale, S. Gordeyev, Shack-Hartmann wavefront sensor image analysis: a comparison of centroiding methods and image-processing, Opt. Eng., Bellingham 52 (7) (2013) 071413.

[39] G. Grimmett, D. Stirzaker, Probability and Random Processes, Oxford University Press, Oxford, England, 2020.

[40] D.M. Winker, G.A. Ameer, S.L. Brown, G.C. Cochran, R. Dueck, D.L. Fried, D.M. Lussier, W. Moretti, P.H. Roberts, K.E. Steinhoff, Characteristics of turbulence measured on a large aperture, in: N.S. Kopeika, W.B. Miller (Eds.), Optical, Infrared, Millimeter Wave Propagation Engineering, 0926, International Society for Optics and Photonics, SPIE, 1988, pp. 360–366.

[41] T.J. Brennan, Anatomy of the slope discrepancy structure function: characterization of turbulence, in: W.E. Thompson, P.H. Merritt (Eds.), in: Laser Systems Technology, vol. 5087, International Society for Optics and Photonics, SPIE, 2003, pp. 103–114.

[42] C.C. Wilcox, C.J. Radosevich, K.P. Healy, A.L. Tuffli, B.D. Agena, M.F. Spencer, D.J.W. III, Digital holography wavefront sensing with a supersonic wind tunnel, in: A. Fimia, M. Hrabovský, J.T. Sheridan (Eds.), Holography: Advances and Modern Trends VI, vol. 11030, International Society for Optics and Photonics, SPIE, 2019, p. 110300L.

[43] M.T. Banet, M.F. Spencer, R.A. Raynor, Digital-holographic detection in the off-axis pupil plane recording geometry for deep-turbulence wavefront sensing, Appl. Opt. 57 (3) (2018) 465–475.

[44] T.J. Bukowski, M. Kalensky, D. Getts, S. Gordeyev, Comparison of shack-hartmann and digital holographic wavefront sensing using a benchtop turbulence generator, in: J.J. Dolne, S.R. Bose-Pillai, M. Kalensky (Eds.), Unconventional Imaging, Sensing, and Adaptive Optics 2024 13149, International Society for Optics and Photonics, SPIE, 2024, 1314910, http://dx.doi.org/10.1117/12.3026892.

[45] M.F. Spencer, Spatial heterodyne, in: B.D. Guenther, D.G. Steel (Eds.), Encyclopedia of Modern Optics, second ed., Elsevier, Oxford, 2018, pp. 369–400, http://dx.doi.org/10.1016/B978-0-12-803581-8.09416-9, URL https://www.sciencedirect.com/science/article/pii/B9780128035818094169.

[46] M.A. Herráez, D.R. Burton, M.J. Lalor, M.A. Gdeisat, Fast two-dimensional phase-unwrapping algorithm based on sorting by reliability following a noncontinuous path, Appl. Opt. 41 (35) (2002) 7437–7444.

[47] A.E. Smith, Evaluation of Passive Boundary Layer Flow Control Techniques for Aero-Optic Mitigation (Ph.D. thesis), University of Notre Dame, 2015, http://dx.doi.org/10.7274/q237hq4074k, URL https://curate.nd.edu/show/q237hq4074k.

[48] A.W. Marsh, T.M. Evans, B.C. Musci, J. Uzodima, S.P. Kearney, D.R. Guildenbecher, Y.C. Mazumdar, Shock-wave distortion cancellation using numerical recalculated intensity propagation phase holography, Opt. Lasers Eng. 146 (2021) 106706.

[49] D. Woodbury, P. Gatt, B.W. Krause, S.T. Thurman, C.A. Noren, M.F. Spencer, Multifunction digital holographic laser remote sensing, in: G.W. Kamerman, L.A. Magruder, M.D. Turner (Eds.), Laser Radar Technology and Applications XXIX, 13049, International Society for Optics and Photonics, SPIE, 2024, 1304903.

[50] M.T. Banet, A. Idris, J.R. Fienup, Multiplexed, Multi-Wavelength 3D Digital Holographic Imaging Methods with Range Unwrapping, International Society for Optics and Photonics, SPIE, 2023, 1269304,

[51] T.C. Khoo, A. Sharikova, A. Khmaladze, Dual wavelength digital holographic imaging of layered structures, Opt. Commun. 458 (2020) 124793.